Am J Cancer Res 2022;12(3):1309-1322
www.ajcr.us /ISSN:2156-6976/ajcr0139547

Original Article

KMT2D loss drives aggressive tumor phenotypes in cutaneous squamous cell carcinoma

Cara Dauch[1], Sharon Shim[2], Matthew Wyatt Cole[1,3], Nijole C Pollock[1], Abigail J Beer[1], Johnny Ramroop[1], Victoria Klee[4], Dawn C Allain[4], Reena Shakya[5], Sue E Knoblaugh[6], Jesse Kulewsky[7], Amanda Ewart Toland[1,4,5]

[1]Department of Cancer Biology and Genetics, The Ohio State University College of Medicine, Columbus, OH 43210, USA; [2]Central Michigan University College of Medicine, Mount Pleasant, MI 48858, USA; [3]Department of Radiation Oncology, The Ohio State University, Columbus, OH 43210, USA; [4]Department of Internal Medicine, Division of Human Genetics, The Ohio State University, Columbus, OH 43210, USA; [5]Comprehensive Cancer Center, The Ohio State University, Columbus, OH 43210, USA; [6]Department of Veterinary Biosciences, The Ohio State University, Columbus, OH 43210, USA; [7]Department of Pathology, The Ohio State University Wexner Medical Center, Columbus, OH 43210, USA

Received October 1, 2021; Accepted February 16, 2022; Epub March 15, 2022; Published March 30, 2022

Abstract: Cutaneous squamous cell carcinoma (cSCC) is the second most lethal skin cancer. Due to ultraviolet light-induced damage, cSCCs have a high mutation rate, but some genes are more frequently mutated in aggressive cSCCs. Lysine-specific histone methyltransferase 2D (*KMT2D*) has a two-fold higher mutation frequency in metastatic cSCCs relative to primary non-metastatic associated cSCCs. The role of KMT2D in more aggressive phenotypes in cSCC is uncharacterized. Studies of other tumor types suggest that KMT2D acts to suppress tumor development. To determine whether KMT2D loss has an impact on tumor characteristics, we disrupted *KMT2D* in a cSCC cell line using CRISPR-cas9 and performed phenotypic analyses. KMT2D loss modestly increased cell proliferation and colony formation (1.4- and 1.6-fold respectively). Cells lacking KMT2D showed increased rates of migration and faster cell cycle progression. In xenograft models, tumors with KMT2D loss showed slight increases in mitotic indices. Collectively, these findings suggest that *KMT2D* loss-of-function mutations may promote more aggressive and invasive behaviors in cSCC, suggesting that KMT2D-related pathways could be targets for cancer therapies. Future studies to determine the downstream genes and mechanism of phenotypic effect are needed.

Keywords: Cutaneous squamous cell carcinoma, cSCC, KMT2D, metastasis, skin cancer

Introduction

Cutaneous squamous cell carcinoma (cSCC) is the second most lethal skin cancer after melanoma, resulting in an estimated 3900-8800 deaths in the United States each year [1, 2]. Unlike SCCs arising in other sites, cSCC has a low rate of metastasis. Two to five percent of primary cSCCs metastasize resulting in an overall 2.1% risk of disease-specific death [2-5]. Aside from recent promising clinical trials of immune checkpoint inhibitors, the majority of treatment options for invasive cSCCs are of low efficacy with a mortality rate of approximately 25-45% for cSCC lymph node metastases and 89% for distant metastases [5]. cSCCs have some of the highest mutation burdens across all tumor types due to ultraviolet radiation (UV)-induced mutations, which may make them more responsive to immune checkpoint inhibitors [6-9]. However, the safety of immune checkpoint inhibitors is not established for individuals with suppressed immune systems, who tend to have more aggressive tumors, and these therapies are not currently recommended for this population [7, 10]. Thus, an understanding of the pathways leading to metastasis in cSCC is important in order to develop new therapeutic approaches.

To identify somatic mutations predictive of metastasis and/or those to aid in design of therapeutic strategies, we and others performed exome and targeted-sequencing studies leading to the identification of genes more commonly mutated in aggressive/metastatic

cSCCs relative to primary non-aggressive cSCCs [11-17]. Many genes showing high mutation rates across all cSCCs were also mutated in a variety of SCC types and were part of a "squamousness" gene signature [18]. Of note, somatic *TP53* variants are more common in aggressive cSCCs compared to non-aggressive cSCCs which has also been reported in head and neck SCCs [19, 20]. Our studies found that *KMT2D*, a gene not included in the squamousness gene signature, had a two-fold higher mutation frequency in aggressive cSCCs (62% of tumors) relative to non-aggressive cSCCs (31%) [17].

KMT2D (also known as *MLL2*) encodes a histone lysine methyltransferase that methylates K4 of histone H3 (H3K4) predominantly in gene enhancers [21]. *KMT2D* is mutated at a high rate in many tumor types, and some have postulated this is due to passenger mutations as it is extremely large (5537 amino acids). Functional studies evaluating the impact of *KMT2D* mutations on tumor phenotypes have been done for a number of cancers including bladder, lung, colorectal, and leukemia. Interestingly, KMT2D expression appears to act to promote more aggressive tumor phenotypes for some cancer types, but for others, it appears to be tumor suppressive [22]. Differences may be due in part to the type of mutation that predominates in the tumors (missense versus nonsense/frameshift) or in total loss versus haploinsufficiency of the protein. Missense mutations in *KMT2D* are associated with more aggressive bladder cancer and a higher expression of the protein. Interestingly, unlike many classic tumor suppressor genes, most cancers with *KMT2D* loss-of-function (LOF) mutations only have a mutation of one allele, suggesting that haploinsufficiency rather than total LOF may be important for driving tumorigenesis [23].

We found *KMT2D* somatic mutations to be much more frequent in aggressive and metastatic cSCCs relative to non-aggressive primary cSCCs, but it is unknown if the difference in frequency was due to a greater mutational burden in the metastatic tumors or if *KMT2D* mutations induce more aggressive phenotypes. The goal of this study was to determine if loss of *KMT2D* expression in cSCC contributes to more aggressive tumor phenotypes in order to determine if this pathway is worthy of studies to identify targeted therapies for metastatic or aggressive cSCC.

Materials and methods

Cell lines

COLO-16 cells were provided by Kenneth Tsai, MD (Moffitt Cancer Center) [24, 25] and cultured in DMEM/F12 supplemented with 10% Fetal Bovine Serum (Gibco; complete medium) with 1% penicillin/streptomycin at 37°C in 5% CO_2. Retroviral packing cell line 293RTV was purchased from Cell Biolabs and grown in DMEM supplemented with 10% Fetal Bovine Serum. COLO-16 cell lines were authenticated by microsatellite genotyping using the Promega GenePrint 10 kit in the Ohio State University Comprehensive Cancer Center Genomics Shared Resource (GSR) prior to phenotypic experiments. Phenotypic experiments were performed at low passages, and all cell lines were tested for mycoplasma regularly.

CRISPR-cas9 knock-out of KMT2D

We utilized a lentiviral system (p.LentiCRISPR v.2) from GenScript. Two different CRISPR-Cas9 plasmids with *KMT2D* guide RNAs X18314 (5' CAGAGAGCACAACGCCGCAC 3') and X18449 (5' CCGACCATGCAGCACACCAA 3') and a control plasmid with no guide RNA (empty vector) were used. Packaging plasmid, pCMF-dR8.2 and envelope plasmid pMD2.D were transfected into 293RTV cells at 70% confluency along with 1 µg of each lentivirus plasmid using Lipofectamine 2000 (ThermoFisher) according to the manufacturer's recommended conditions. Eighteen hours post-transfection, transfection media was exchanged for high growth media (DMEM with 30% FBS). Viral supernatant was collected every 6-12 hours over the next 24 hours. After collection was complete, viral supernatant was spun at 1250 rpm for 5 minutes and supernatant filtered through a 0.45 µM syringe filter. A 1:1 mixture of viral supernatant and growth media with polybrene (8 µg/ml) was added to cells plated at 70% confluency. The viral supernatant/media mixture was replenished after 6 hours. Approximately 24 hours post-transduction, media was replaced with regular growth media plus puromycin (1 µg/ml). Media with puromycin was replenished every 3 days until about 10 days. Surviving cells were plated

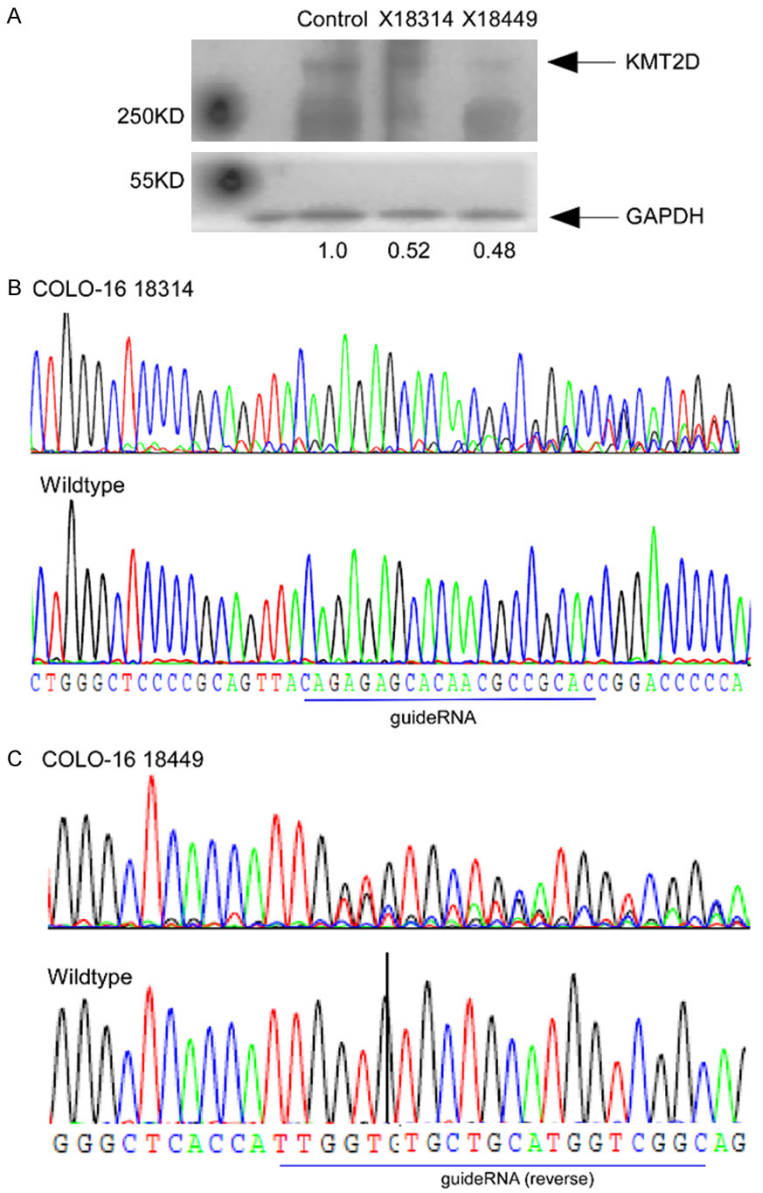

Figure 1. KMT2D knockdown using CRISPR-Cas9. (A) Western blot of KMT2D protein expression from COLO-16 control and two KMT2D knockdown cell lines (X18314 and X18449). The ratios of KMT2D protein levels relative to GAPDH are shown. Sanger sequencing data for *KMT2D* wildtype and knockdown cells at the location for guideRNA X18314 (B) and X18449 (C) are shown. Guide RNAs are denoted with a blue line.

as single colonies in regular growth media. *KMT2D* knockdown was confirmed by RT-qPCR and normalized to *HPRT* expression (data not shown). Clones with knockdown by cDNA expression were sequenced verified using Sanger sequencing and by western for knockdown of protein (**Figure 1**). One clone of each CRISPR-cas9 guide per cell line was chosen for phenotypic studies.

Western analysis

Protein from whole cell extracts was extracted using RIPA buffer (500 µl 1 M Tris base pH 8, 300 µl 5 M NaCl, 1 mL 10% NP40, and 100 µl 10% SDS) and 25X protease inhibitor (Roche). Typically, 30 µg of protein was run on 7% SDS-PAGE gels in a Bio-Rad mini-gel system at 150 volts for approximately 90 minutes. Protein was transferred onto nitrocellulose membrane (Amersham Protan, 0.45 um, #10600008) 4°C overnight at 45 volts. Following overnight transfer, the membrane was blocked using 5% milk in TBST (10× TBS: 1.2% Tris, 8.8% NaCl) for 2 hours. Primary antibody incubations were completed overnight at 4°C. Primary antibody dilutions were: KMT2D primary antibody (ThermoFisher Scientific, Anti-KMT2D, PA5-57-490) 1:500, and GAPDH (Invitrogen, AM4300) 1:2500. Following washes with 1× TBST (100 mL 10× TBS, 1 mL Tween 20, 900 mL dH_2O), membrane was incubated with secondary antibody for 2 hours. Secondary antibody and dilution was as follows: anti-rabbit IgG, HRP-linked antibody (Cell Signaling, #70-74) 1:5000. SuperSignal Pico-PLUS chemiluminescent substrate (Thermo Scientific) was added at a 1:1 ratio. Protein signal was visualized using a Li-Cor Odyssey Fc. Protein bands were quantified using ImageJ software.

Sanger sequencing

To determine the exact site of *KMT2D* mutations generated using CRISPR, PCR products using primers flanking the expected cut site were treated with ExoSAP-IT (ThermoFisher)

according to manufacturer's recommended conditions and were sent to the GSR for Sanger sequencing. Sequence traces were analyzed using SeqmanPro16 from the DNAStar LaserGene17 software package.

Proliferation

Proliferation was measured by 3-(4,5-dimethylthiazol-2-yl)-2,5-diphenyl tetrazolium bromide, MTT, Cell Proliferation Kit I (Roche) per manufacturer's recommended conditions. Four thousand cells per well were plated in a 96 well plate (CellStar) in quadruplicate. Each plate was read in a Biotek Synergy 2 microplate reader at wavelengths of 550 and 670 nm at time points 0, 24, 48, 72 and 96 hours post-plating at multiple times during this study. Cells were also tested for mycoplasma and were mycoplasma free. Negative controls included media only. The absorbance value provided by the blanks was subtracted by the absorbance value for the samples. The percent cell viability was calculated by dividing the value of absorbance for treated cells by the value of absorbance for control cells and then multiplying by 100.

Clonogenic cell colony formation

A clonogenic cell colony formation assay was carried out by plating 500 cells per well in triplicate in a 6-well cell culture plate (Greiner bio-one Cellstar). Seven days post-plating, cells were fixed for 10 minutes using 2 mL of fixing buffer (1 part acetic acid to 7 parts methanol) and stained in 2 mL 0.5% Crystal violet diluted in 10% methanol for 30 minutes. Excess crystal violet was removed, the plates were washed with water and air-dried. Prior to destaining photos were taken using the ProteinSimple FluorChemE imaging system. For experiments in which there were distinct colonies, colonies were counted manually from the photos by two blinded reviewers. Averages and standard deviation across the triplicate platings of each condition were calculated. Colonies were destained on a shaker using 1 mL of 100% methanol for 1 hour. To quantify staining intensity, 150 µl of supernatant from each well was added in triplicate to a 96 well optically clear plate. Plates were read at 580 nm on a SPECTRAmax M2 spectrophotometer (Molecular Devices).

Apoptosis

Apoptosis was measured using a FITC Annexin V Apoptosis Detection Kit I (BD Pharmingen™) according to the manufacturers recommended conditions. Cells were harvested and trypsinized using 0.25% Trypsin (Corning). Cells were counted and resuspended in 1× Binding Buffer at a concentration of 1×10^6 cells/mL. In a 5 mL culture tube, 5 µl of FITC Annexin V and 5 µl of propidium iodide (PI) was added to 100 µl of cell suspension. Cells were vortexed and incubated for 15 minutes in the dark, at room temperature (RT). After incubation, 400 µl of 1× Binding Buffer was added. Samples were analyzed immediately by flow cytometry on a BD LSRFortessa™. Gates were created for Annexin V^-/PI^- (quadrant 3, viable cells), Annexin V^+/PI^- (quadrant 2, early apoptotic cells), Annexin V^+PI^+ (quadrant 4, late apoptotic necrotic cells), and Annexin V^-PI^+ (quadrant 1, late necrotic cells). Cell numbers in quadrant 2 and quadrant 4 were combined to determine the percentage of cells in early and late apoptosis.

Cell cycle analysis

Cells were trypsinized using 0.25% Trypsin (Corning) and washed once with PBS. After washing, 500 µl of ice cold 70% EtOH was added dropwise while vortexing at a low speed. Cells were then incubated for 10 minutes on ice, spun down at 800× g, and resuspended in 100 µl RNase-A-PBS (180 vg/ml, Pharmacia). Cells were incubated at RT for 30 minutes. Following incubation, 200 µl PI-PBS (75 µg/ml, GBiosciences) was added to a final concentration of 50 µg/ml and total volume of 1×10^6 cells in 300 µl. Following a 15 minute RT incubation period suspensions were analyzed by flow cytometry on a BD LSRFortessa™ in the Analytic Cytometry Shared Resource.

Cell migration

Cell migration assays were performed using 33 mm two-well culture inserts (Ibidi, Fitchberg, WI). Inserts were placed in a 60 mm ×15 mm cell culture dish (Corning Incorporated, Corning NY). For each experiment, 70 µl of media with 1% serum containing 49,000 cells was plated on each side of the insert and incubated at 37°C overnight. The following morning, inserts were removed, and migration was visualized by microscope until a separation between the two sides of the insert in at least one of the experimental groups could no longer be seen. Each sample was plated in duplicate and each experiment was repeated in triplicate.

Xenograft models

All animal studies were approved by the Ohio State University Animal Care and Use Committee. Outbred athymic nude mice (NCr-nu/nu) were acquired from the athymic nude mouse colony maintained by the OSU Comprehensive Cancer Center (CCC) Target Validation Shared Resource (TVSR). Original breeders (strain# 553 and 554) for the colony were obtained from NCI Frederick/Charles River. Animals were housed in individually ventilated, sterile cages with Bed-o-cobs under 12 hour light-dark cycle; they were provided Envigo-Teklad rodent diet, 7912, and reverse-osmosis water *ad libitum*. Female mice aged 6-7 weeks of age were injected subcutaneously into both right and left flanks with 2×10^6 cells resuspended in 100 µl PBS with 50 µl of matrigel (Corning) per injection site. Cells were harvested and trypsinized using 0.25% trypsin (Corning), washed twice with cold PBS and counted using the Countess II automated cell counter (ThermoFisher). Following resuspension in PBS, samples were kept on ice until injection. Groups consisted of 13 animals injected with control COLO-16 cells, 14 animals injected with X18314 cells and 13 animals injected with X18449 cells. Tumors became visible beginning at 6 days post-injection and were measured with calipers at days 6, 9, 13, and 16 post-injection. Mice were humanely euthanized via CO_2 asphyxiation followed by cervical dislocation at 16 days post-tumor-cell injection as mice in all groups were losing weight and appeared cachexic. Tumors were harvested and divided into two pieces with one-half snap frozen in liquid nitrogen and the other half fixed in 10% neutral buffered formalin.

Histopathology and immunohistochemistry

Histological preparation hematoxylin and eosin (H&E) and immunohistochemical (IHC) staining was performed by the Ohio State University Comparative Pathology & Digital Imaging Shared Resource (CPSIDR). A representative group of eight tumors from each of the three groups were processed by routine methods and embedded in paraffin wax. Sections (4 µm) were stained with H&E and evaluated with a Nikon Eclipse Ci (Nikon Instruments, Melville New York) with attached Olympus SC50 digital camera (B and B Microscropes Limited, Pittsburgh, PA) by a veterinary pathologist certified by the American College of Veterinary Pathologists (SEK). H&E sections were evaluated visually for tumor morphology, immune cell infiltration, and angiogenesis. The mitotic rate and percent of necrosis were reported using three random 40× magnification high power fields. Immunohistochemical staining for CD31 and Ki-67 was completed on the same set of tumors. Four µm sections were stained for CD31 (1:100; polyclonal rabbit, catalog number 28362, Abcam) and Ki-67 (1:100; polyclonal rabbit [Clone SP6], catalog number RM9106, ThermoScientific) on a Thermo360 autostainer. Antigen retrieval was performed in Citrate pH 6 solution (Dako, S1699) pre-heated to at least 96°C using a steamer. Slides were incubated with a biotinylated goat anti-rabbit diluted secondary antibody at 1:200 (Vector, BA-1000) Secondary Antibody diluted in Serum Free (Dako, S3022) for 30 minutes and detected with Vector ABC HRP RTU Elite (Vector, PK-7100) and DAB chromagen. Negative controls included omission of primary antibody and isotype-matched controls by using non-specific IgG at concentrations similar to those for the respective primary antibodies.

Image analysis

Slides immunostained for Ki-67 were scanned at 40X with a Leica Aperio ScanScope XT high-resolution scanner (Leica Biosystems Buffalo Grove, IL) at the CPSIDR. For the quantification of immunoreactivity, images were imported into Visiopharm Image Analysis software (Visiopharm, Hørsholm, Denmark version 2018.09). Images were segmented into areas of tumor, and areas of necrosis, adipose, and slide artifacts, such as folds, were eliminated. Ki-67 positive and negative nuclei were scored using the Visiopharm APP 1004-Ki-67, Breast Cancer. Positive nuclei were labeled red and negative nuclei were labeled blue. The total nuclei per section, total Ki-67 positive nuclei, total Ki-67 negative nuclei were calculated. The average proliferation index was calculated as total Ki-67 positive nuclei divided by total nuclei X100. Initial thresholds and tissue types were established and mark-ups reviewed in consultation with a veterinary pathologist (SEK) to ensure accurate measurements and differentiate between tissue types.

AR-42 treatment

Stock solutions of AR-42 were prepared in DMSO to concentrations of 10 mM/mL. COLO-16 control and knockdown cells (10,000 each) were plated in a 96-well plate overnight. Cells were treated with vehicle control, DMSO, or AR-42 at 0.01, 0.1, 0.5, and 1.0 μM and incubated for 24 hours. Cell viability was analyzed using an MTT assay.

Statistical analyses

Experiments were performed at least 3 times with three replicates per experiment except as noted. The standard deviations of the mean of the three replicates are presented for MTT, apoptosis, cell cycle, and clonogenic assays. GraphPadPrism software (v.7) was used to perform Student t-tests for clonogenic and MTT assays. *P*-values of less than 0.05 were considered significant.

Results

Loss of KMT2D promotes growth of cSCC cells

Somatic mutations in *KMT2D* are twice as frequent in metastatic or aggressive cSCCs compared to primary cSCCs that did not metastasize [17]. However, the literature describing *KMT2D* as a tumor suppressor or oncogene is mixed. To study the effects of the loss of KMT2D on cancer and metastasis-related phenotypes, we knocked-down expression KMT2D expression in COLO-16, a cSCC cell line, using CRISPR-Cas9. Two unique *KMT2D* guide RNAs, X18314 and X18449 were used to generate different knockdown clones to decrease the probability that observed results were due to off-target effects. Single colonies with reduced KMT2D protein expression were selected for down-stream functional studies (**Figure 1A**). Exact mutations were confirmed using Sanger sequencing (**Figure 1B**, **1C**).

To determine if loss of KMT2D affects proliferation or growth as single colonies, we performed MTT and clonogenic assays. Proliferation of the KMT2D knockdown lines, X18314 and X18449, was modestly increased in comparison to control COLO-16 cells under normal growing conditions (**Figure 2A**). The average fold increased proliferation compared to control cells at 72 hours post plating was 1.5 and 1.7 for COLO-16, X18314, and X18449 (*P*-values ≤0.001). In concordance with a faster proliferation rate, colony formation assays, completed over 7 days, demonstrated that KMT2D knockdown increased colony formation as measured by absorbance (**Figure 2B**), visual imaging (**Figure 2C**) and manual counting (**Figure 2D**) with X18314 and X18449 showing approximately 1.5 and 3.5-fold increased colony formation by manual counts (*P*-value 0.011 and 0.006, respectively) (**Figure 2B-D**).

Loss of KMT2D modestly decreases levels of apoptosis

To determine if loss of KMT2D had an impact on apoptosis, cells were stained with Annexin V/Propidium Iodide and sorted. Compared to COLO-16 control cells, X18314 showed no significant differences in apoptosis and X18449 had a 1.5-fold decrease in the proportion of early and late apoptotic cells (*P*-values 0.0005) (**Figure 3A**).

KMT2D loss leads to modest increases in cells in G2/M

To determine if loss of KMT2D resulted in changes in cell cycle progression, cell cycle analysis of unsynchronized cells was completed. Compared to COLO-16 control cells, a slightly higher percentage of X18314 and X18449 cells were in S (10.7% and 9.8% versus 6.7%, *P*-values ≤0.001) and in G2/M (14.2% and 12.4% versus 9.9%, *P*-values ≤0.001), and fewer KMT2D knockdown cells were in G0/G1 (73.1% and 74.5% versus 82.1%, *P*-values 0.003 and 0.01) (**Figure 3B**). These data suggest that loss of KMT2D leads to modes increases in cell cycle progression and are consistent with the observed modest increases in proliferation.

Loss of KMT2D promotes cell migration

To measure the impact of KMT2D loss on cell migration, a scratch assay was performed. The scratch closed in both COLO-16 knockout cell lines in about 8-12 hours, compared to over 12 hours for the COLO-16 control cell line (**Figure 4** and data not shown).

In vivo models reveal modest phenotypic differences

To study the impact of KMT2D loss *in vivo*, xenograft studies were performed. COLO-16 control and knockdown cell lines were injected

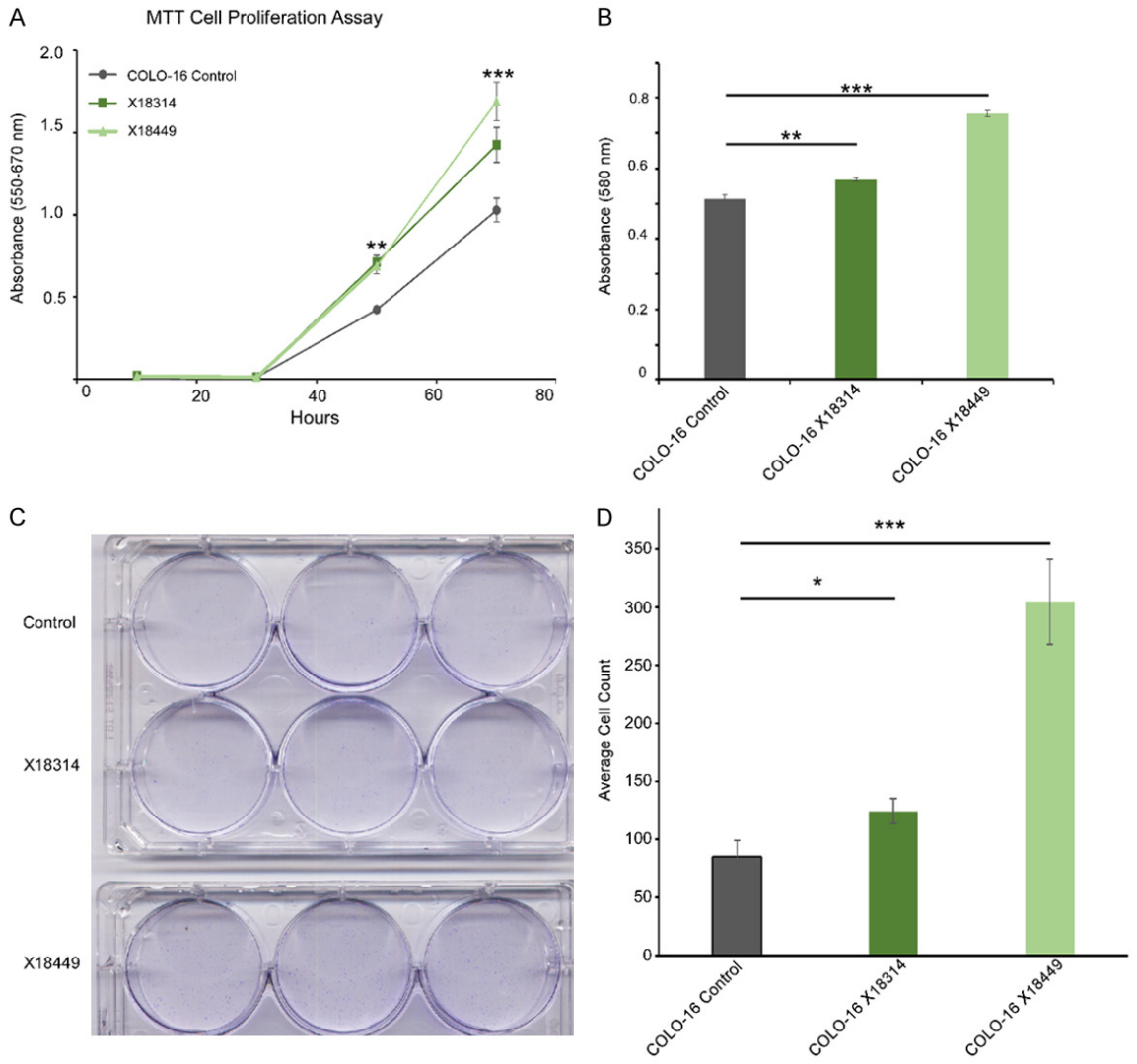

Figure 2. Decreased KMT2D increases proliferation and colony formation. Representative data from a MTT cell proliferation assay is shown for (A) COLO-16 control, X18314, and X18449 cells represented by circles, squares, and triangles, respectively. (B) Quantitation of destained crystal violet staining of clonogenic assays of cells in a 6-well plate for COLO-16 control (gray), X18314 (dark green) and X18449 (light green) is shown. (C) Representative images of colonies for COLO-16, X18314, X18449 are shown. (D) Average manual counts of cells for colonies in (C). Samples were run in quadruplicate for MTT assays and in triplicate for clonogenic assays. Experiments were run three times. Error bars represent standard deviation, $^{*}P\leq0.05$, $^{**}P\leq0.01$, $^{***}P\leq0.001$.

subcutaneously on both left and right flanks of NCr-nu/nu mice. At 6 days post-tumor cell inoculation, tumors became palpable. The average tumor volumes at six days for control, X18314, and X18449, were 148 mm^3, 175 mm^3, and 155 mm^3 respectively (**Figure 5A**). At 16 days post-tumor cell inoculation, the mice had to be euthanized due to extreme loss of body weight. At the time of sacrifice, tumor sizes for control, X18314, and X18449 were 614 mm^3, 637 mm^3, and 754 mm^3 (**Figure 5A**); average tumor weights were 0.35, 0.43, and 0.46 grams respectively. Differences in tumor weights and volumes were not significantly different (*P*-values 0.15 and 0.18); however the percent tumor volume change between day 6 and 16 was significantly different between X18449 and control (*P*-value 0.03) (**Figure 5B**).

Representative H&E stained sections from eight tumors from COLO-16 control, X18314, and X18449 xenograft mice were evaluated by a veterinary pathologist (SEK). KMT2D knockdown was confirmed by western (data not shown). Morphology across tumors was consistent with squamous cell carcinoma and was

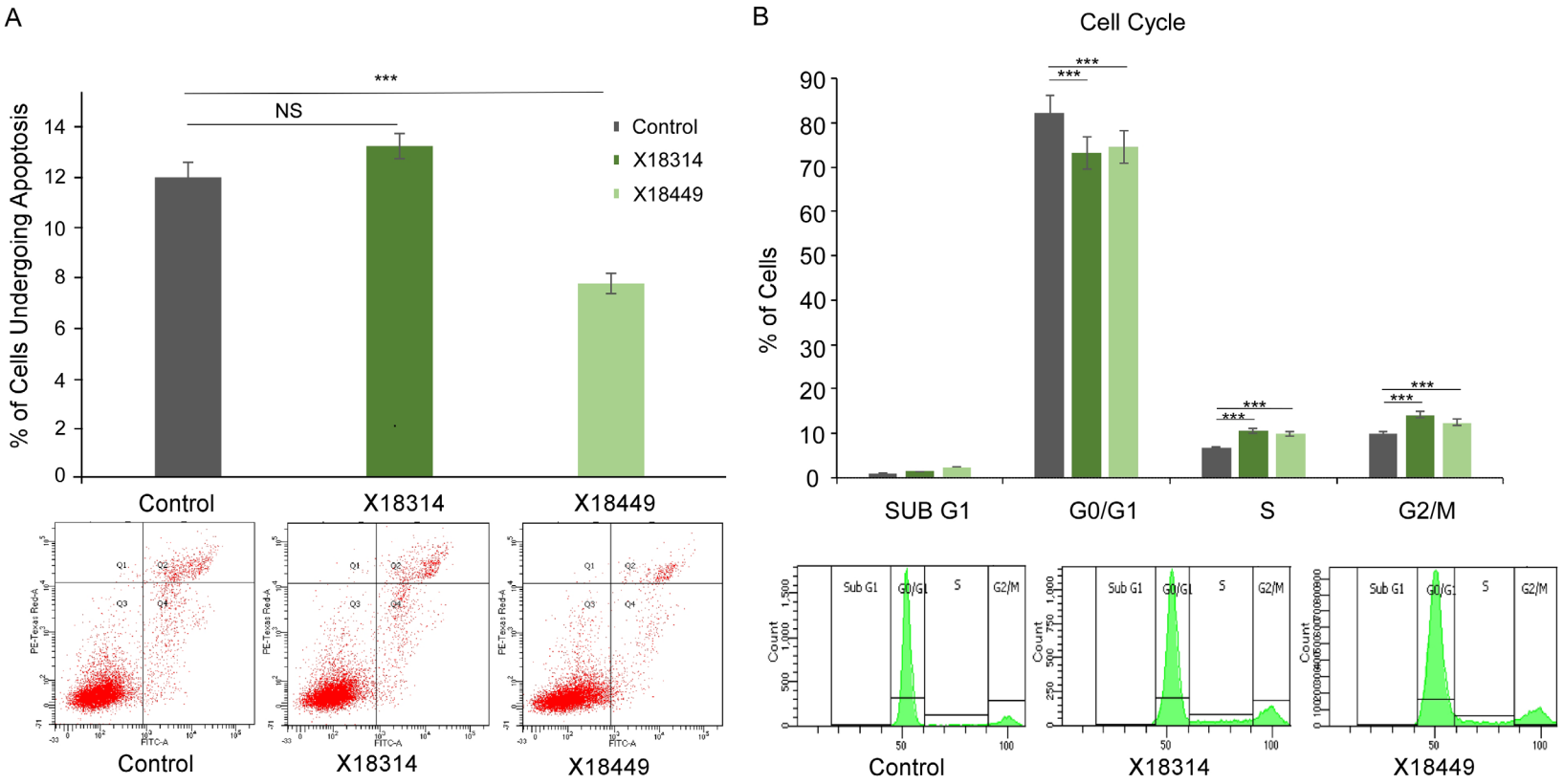

Figure 3. KMT2D knockdown reduces apoptosis and increases cell cycle. A. The percentage of cells staining positive for Annexin V (quadrant 2 and quadrant 4) of COLO-16 control (gray) and KMT2D knockdowns X18314 (dark green) and X18449 (light green) is shown with representative FACS plot for each condition. B. The percentage of cells in each phase of the cell cycle for COLO-16 control (gray) X18314 (dark green) X18449 (light green) cells are plotted with representative FACS analyses for each condition. Error bars represent standard deviation, $^{*}P\leq0.05$, $^{**}P\leq0.01$, $^{***}P\leq0.005$. Samples were run in triplicate and experiments were run three times.

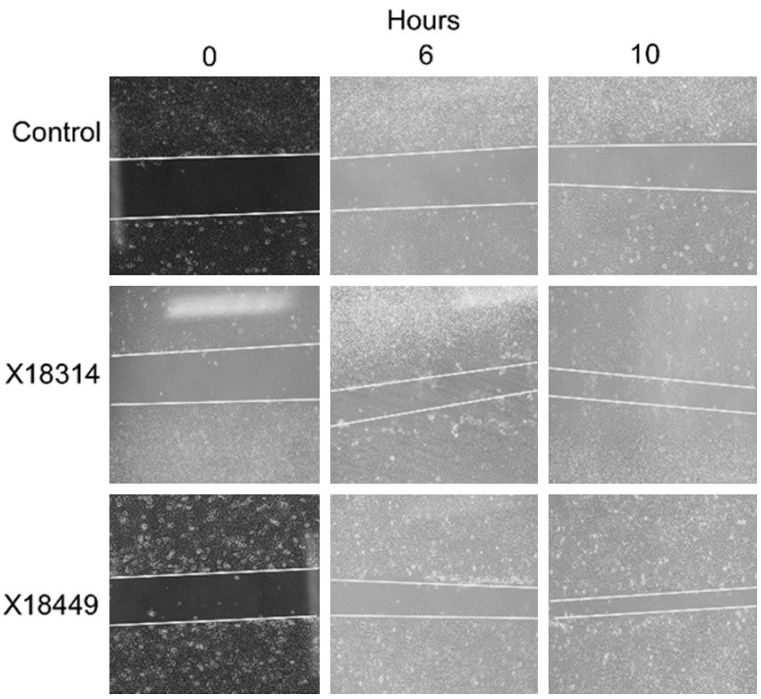

Figure 4. KMT2D knockdown enhances cell migration. Scratch assays for COLO-16 control and knockdown cell lines X18314 and X18449 cell lines at 0, 6 and 10 hours are shown. White lines highlight the size of the gap. Samples were run in duplicate and experiments were run three times.

similar between the three experimental groups (**Figure 5C**). Average mitotic rates for control, X18314, and X18449 were 9.9, 11.0, and 13.9 in three random 40× high power field of view, respectively (data not shown). There was a high degree of tumor necrosis observed in all groups with an average percentage of necrosis of 26%, 25%, and 36% for control, X18314 and X18449. Large areas of necrosis may be secondary to rapid growth of the xenografts. Immunohistochemistry for CD31 was performed to evaluate for angiogenesis. Although not significant, vessel counts in three random 40X high power fields for control, X18314, and X18449 tumors showed slight differences with mean values of 9.62, 12.24, and 12.79, respectively (*P*-value 0.18 and 0.18, respectively; **Figure 6**). Immunohistochemistry for Ki-67 was also performed, and quantification via image analysis was performed on whole slide images to measure proliferation. There was a large number of Ki-67 positive nuclei noted for all three experimental groups. The proliferation index was measured via image analysis, and average percentages were 94.06, 88.78, and 90.13, respectively (*P*-values 0.07 and 0.11).

Therapeutic treatment

Pathogenic LOF germline variants in *KMT2D* cause Kabuki syndrome, an autosomal dominant developmental disorder characterized by intellectual disability, immunological defects, dysmorphic features, congenital heart defects and other anomalies [26, 27]. Individuals with Kabuki syndrome exhibit a unique genomic methylation pattern indicative of haploinsufficiency of protein activity. Mouse models of Kabuki syndrome have found that histone deacetylase inhibition via agent AR-42 restored some of the neurological defects and partially restored histone 4 acetylation and histone H3K4 trimethylation in mouse embryonic fibroblasts isolated from these mice [28, 29]. These data suggest the possibility of targeting this pathway in tumors with reduced KMT2D activity.

To determine if AR-42 could reverse the phenotypic effects of KMT2D loss in COLO-16 cells, we treated COLO-16 control and KMT2D knockdown cells with a range of doses of AR-42. The COLO-16 control and both COLO-16 KMT2D knockdown cells were exquisitely sensitive to treatment by AR-42 at doses of 0.01, 0.1, 0.5, and 1.0 μM and died within 24 hours (data not shown). Cells treated with vehicle control (DMSO) survived. As all cells treated with all doses of AR-42 died, these data suggest that COLO-16 cells have another vulnerability that makes them sensitive to AR-42 independent of KMT2D status.

Discussion

KMT2D is one of the most frequently mutated genes in metastatic cSCC with approximately 62% of metastatic cSCCs containing mutations [17]. Here, we show evidence that loss of KMT2D *in vitro* leads to more aggressive tumor phenotypes of cSCC cell lines including increased migration, rates of proliferation, and

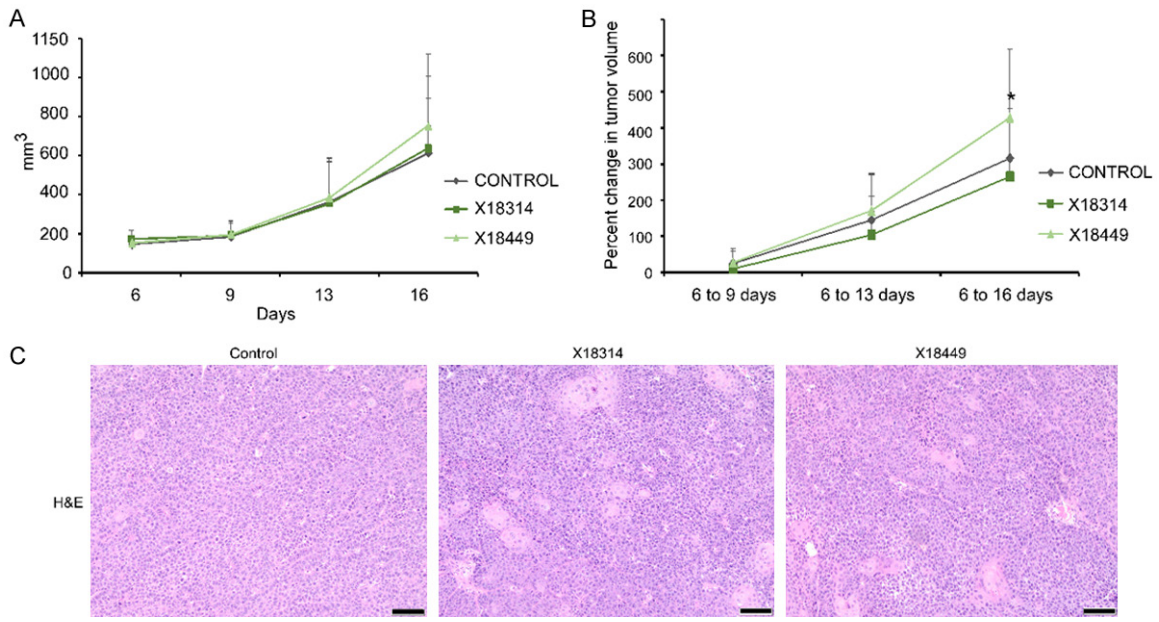

Figure 5. Xenograft tumor growth and staining. A. The average tumor volume for control (gray) and knockdown xenograft cell lines X18314 (dark green) and X18449 (light green) at 6, 9, 13 and 16 days post-injection is shown. B. The percent change in tumor volume between 6 and 9, 6 and 13, and 6 and 16 days post-injection is shown for control (gray) and knockdown xenograft cell lines X18314 (dark green) and X18449 (light green). C. Representative 10× magnification images of control COLO-16 and knockdown xenograft X18314 and X18449 xenograft tumors stained with Hematoxylin and Eosin; bar 100 μm; *P≤0.05.

clonogenic growth. These data are consistent with KMT2D acting to suppress tumor development in cSCC.

From the literature, the effects of KMT2D loss in tumors vary and are cancer type specific. Our results show that in skin cancer, KMT2D functions to suppress tumor phenotypes. In bladder cancer, the silencing of KMT2D significantly increases cell viability, migration and invasion similarly to our results in the cSCC cell lines. Overexpression of KMT2D in bladder cancer cells was shown previously to have opposite results and promote tumor suppressive phenotypes [30]. In breast cancer, *KMT2D* mutations leading to low KMT2D levels are associated with poor survival [31]. Surprisingly, the opposite is true in gastric and prostate cancer cells. Knockdown of *KMT2D* suppresses cell proliferation and increases apoptosis in both of gastric and prostate cancer cell lines [32, 33], and overexpression of *KMT2D* is associated with worse prognosis in the gastric cancer cells [33]. One explanation of why *KMT2D* mutations may cause large variations in tumor phenotype dependent on tissue type could be KMT2D's relation to NOTCH signaling. In skin tumors, NOTCH protein acts to suppress tumors. This is also true in bladder cancer [34]. Conversely, NOTCH acts as an oncogene in gastric cancer [35] as well as in leukemia and lymphomas. Since KMT2D knockdown leads to tumor suppression in gastric cancer, suppression could be caused by decreased NOTCH signaling, as NOTCH uses KMT2D for gene activation. NOTCH signalling is active during adult tissue homeostasis and can control transcriptional responses in cellular functions such as proliferation, migration, survival, and fate specification [36]. NOTCH-dependent gene activation requires the displacement of the NCoR/HDAC complex, which is facilitated by KMT2D, and results in full gene activation. When *KMT2D* is mutated or expression is lost, this gene activation may not occur resulting in an imbalance of NOTCH signaling. In Kabuki syndrome, one *KMT2D* allele is mutated causing hyper-activated NOTCH signaling [37]. The relationship between KMT2D and the NOTCH signaling pathway in cSCC needs further exploration.

Our data are consistent with tissue-specific roles for KMT2D in the skin. Previous studies of primary undifferentiated epidermal keratinocytes showed that *KMT2D* shRNA leads to reduced expression of genes important in the

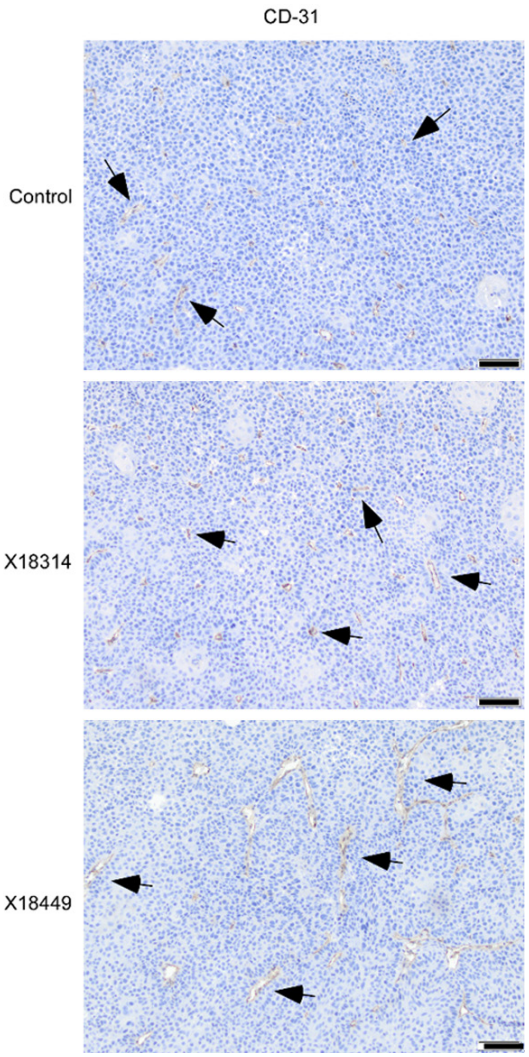

Figure 6. CD-31 staining. Representative 10× magnification images of control COLO-16 and knockdown xenograft X18314 and X18449 xenograft tumors stained with CD-31 (brown). Arrows show a subset of cells staining positively for CD-31; bar 100 μm.

epidermal basement membrane such as *COL4A2*, *LAMB2*, and *LAMA5* as well as those important in cellular adhesion, migration, and the extracellular matrix [38]. These genes are all targets of KMT2D binding to consensus p63-binding site elements. P63 is a critical transcription factor in the skin. Loss of the most highly enriched KMT2D/TP63 target gene, vitamin D receptor (*VDR*), increases metastatic or invasive potential for breast, epidermoid, and renal cell carcinoma cell lines [38-41]. These findings are in alignment with our data showing that KMT2D loss in cSCC cell lines leads to increased migration rates and our previous data showing aggressive tumors are more likely to have *KMT2D* mutations than tumors that do not metastasize [17]. Further exploration of *VDR* as well as p63-KMT2D and p53-KMT2D enhancer networks may help to explain some of the differential tumor-specific effects of *KMT2D* loss between tumor types.

Strengths of our study design are that all *in vitro* assays were completed in isogenic COLO-16 cell lines and showed consistent results. The use of two different *KMT2D* gRNAs for CRISPR-Cas9 mediated gene knockout reduces potential off-target CRISPR-cas9 effects. All assays were completed with biological replicates in triplicate, and each assay was repeated at least three times. There are some limitations to this study. Studies were only done using one cell line. Additionally, the xenograft experiments needed to be terminated early due to unexpected weight loss observed in the mice so longer-term effects on tumor size and phenotypes were unable to be assessed. Although the xenograft models also did not show conclusive differences, there were trends of higher mitotic indices and larger tumor size and rate of growth for the X18449 line. For some phenotypes, such as apoptosis and growth of xenografts, X18314 cells were more similar to control cells than to X18449 cells. There are a couple of potential explanations for the observed heterogeneity of the two different KMT2D knock-down lines including potential non-identified off target effects of the guideRNA for X18449 leading to decreased apoptosis and subsequent higher growth in mice. It is also possible that there is heterozygous rather than homozygous KMT2D expression in the X18314 line that affected some phenotypes more than others.

We did not examine the impact of KMT2D loss on angiogenesis which could be relevant. A study by Serrano et al. showed that KMT2D loss led to defects in angiogenesis in zebrafish, specifically abnormal aortic arch development and hyperactive blood vessel sprouting. The results of this study suggested that KMT2D plays a role in the regulation of angiogenesis, and suggests that the angiogenesis defects are caused by a disruption in the NOTCH pathway when a KMT2D mutant is present [37]. Disruption in the NOTCH pathway could help explain the increased levels of survival we saw in our study. KMT2D has also been shown to impact metabolism, which was not examined in

our study. Other studies have found that loss of KMT2D causes a cell bioenergetics deficiency, specifically causing reduced resting mitochondrial respiratory activity [42]. These results suggest that KMT2D may have a role in controlling aerobic metabolism. The mechanism of this is unknown, but the findings help explain why KMT2D haploinsufficiency can lead to the onset of Kabuki syndrome through a re-wiring of the mitochondrial metabolic phenotype.

Here, we evaluated the impact of loss of KMT2D expression in promoting tumor phenotypes in cSCC. We showed that loss of KMT2D in a cSCC cell line led to increased proliferation, cell colony growth, migration, and accelerated progression through the cell cycle *in vitro*. The KMT2D knockdown xenograft models showed a slight but non-significant increase in overall tumor volume. To determine the mechanism by which loss of KMT2D promotes tumor growth, future studies examining pathways and gene expression impacted by KMT2D loss are critical. Further exploration of the p63-KMT2D and p53-KMT2D enhancer networks as well as impact of loss of KMT2D on the NOTCH pathway in the skin may also be beneficial in explaining the differential tumor-specific effects of *KMT2D* loss between different tumor types and may uncover new strategies for treating aggressive cSCC.

Acknowledgements

The OSU CCC GSR ran qPCR plates, provided Sanger sequencing support, and performed genotyping for cell line authentication. The TVSR provided support for xenograft studies. All FACS analyses were done in the OSU CCC Analytic Cytometry Shared Resource. We acknowledge the CPDISR for histology and immunohistochemical support. We thank Dr. Kenneth Tsai for providing the COLO-16 cell line. Shreya Ghanekar and Aarshvi Bhatt provided experimental assistance. Funding for this study includes grants from the National Institutes of Health (P30 CA016058), a Pelotonia Postdoctoral Fellowship (to J.R.), a Pelotonia Idea Award (to A.E.T.) and a Kenyon College-OSU CCC Summer Fellowship (to M.W.C.).

Disclosure of conflict of interest

None.

Address correspondence to: Amanda Ewart Toland, Department of Cancer Biology and Genetics, The Ohio State University College of Medicine, Columbus, OH 43210, USA. Tel: 614-247-8185; Fax: 614-688-8675; E-mail: amanda.toland@osumc.edu

References

[1] Rogers HW, Weinstock MA, Harris AR, Hinckley MR, Feldman SR, Fleischer AB and Coldiron BM. Incidence estimate of nonmelanoma skin cancer in the United States, 2006. Arch Dermatol 2010; 146: 283-287.

[2] Karia PS, Han J and Schmults CD. Cutaneous squamous cell carcinoma: estimated incidence of disease, nodal metastasis, and deaths from disease in the United States, 2012. J Am Acad Dermatol 2013; 68: 957-966

[3] Schmults CD, Karia PS, Carter JB, Han J and Qureshi AA. Factors predictive of recurrence and death from cutaneous squamous cell carcinoma: a 10-year, single-institution cohort study. JAMA Dermatol 2013; 149: 541-547.

[4] Rees JR, Zens MS, Celaya MO, Riddle BL, Karagas MR and Peacock JL. Survival after squamous cell and basal cell carcinoma of the skin: a retrospective cohort analysis. Int J Cancer 2015; 137: 878-884.

[5] Brunner M, Veness MJ, Ch'ng S, Elliot M and Clark JR. Distant metastases from cutaneous squamous cell carcinoma-analysis of AJCC stage IV. Head Neck 2013; 35: 72-75.

[6] Migden MR, Rischin D, Schmults CD, Guminski A, Hauschild A, Lewis KD, Chung CH, Hernandez-Aya L, Lim AM, Chang ALS, Rabinowits G, Thai AA, Dunn LA, Hughes BGM, Khushalani NI, Modi B, Schadendorf D, Gao B, Seebach F, Li S, Li J, Mathias M, Booth J, Mohan K, Stankevich E, Babiker HM, Brana I, Gil-Martin M, Homsi J, Johnson ML, Moreno V, Niu J, Owonikoko TK, Papadopoulos KP, Yancopoulos GD, Lowy I and Fury MG. PD-1 blockage with cemiplimab in advanced cutaneous squamous cell carcinoma. N Engl J Med 2018; 379: 341-351.

[7] Gellrich FF, Hüning S, Beissert S, Eigentler T, Stockfleth E, Gutzmer R and Meier F. Medical treatment of advance cutaneous squamous-cell carcinoma. J Eur Acad Dermatol Venereol 2019; 33 Suppl 8: 38043.

[8] Goodman AM, Kato S, Chattopadhyay R, Okamura R, Saunders IM, Montesion M, Frampton GM, Miller VA, Daniels GA and Kurzrock R. Phenotypic and genomic determinants of immunotherapy response associated with squamousness. Cancer Immunol Res 2019; 7: 866-873.

[9] Nagarajan P, Asgari MM, Green AC, Guhan SM, Arron ST, Proby CM, Rollison DE, Harwood CA

and Tolan AE. Keratinocyte carcinomas: current concepts and future research priorities. Clin Cancer Res 2019; 25: 2379-2391.

[10] Willenbrink TJ, Jambusaria-Pahlajani A, Arron S, Seckin D, Harwood CA and Proby CM. Treatment approaches in immunosuppressed patients with advance cutaneous squamous cell carcinoma. J Eur Acad Dermatol Venereol 2019; 33 Suppl 8: 57-60.

[11] Wang NJ, Sanborn Z, Arnett KL, Bayston LJ, Liao W, Proby CM, Leigh IM, Collisson EA, Gordon PB, Jakkula L, Pennypacker S, Zou Y, Sharma M, North JP, Vemula SS, Mauro TM, Neuhaus IM, Leboit PE, Hur JS, Park K, Huh N, Kwok PY, Arron ST, Massion PP, Bale AE, Haussler D, Cleaver JE, Gray JW, Spellman PT, South AP, Aster JC, Blacklow SC and Cho RJ. Loss-of-function mutation in Notch receptors in cutaneous and lung squamous cell carcinoma. Proc Natl Acad Sci U S A 2011; 108: 17761-17766.

[12] South AP, Purdie KJ, Watt SA, Haldenby S, den Breems N, Dimon M, Arron ST, Kluk MJ, Aster JC, McHugh A, Xue DJ, Dayal JH, Robinson KS, Rizvi SH, Proby CM, Harwood CA and Leigh IM. NOTCH1 mutations occur early during cutaneous squamous cell carcinogenesis. J Invest Dermatol 2014; 134: 2630-2638.

[13] Lee CS, Bhaduri A, Mah A, Johnson WL, Ungewickell A, Aros CJ, Nguyen CB, Rios EJ, Siprashvili Z, Straight A, Kim J, Aasi SZ and Khavari PA. Recurrent point mutations in the kinetochore gene KNSTRN in cutaneous squamous cell carcinoma. Nat Genet 2014; 46: 1060-1062.

[14] Pickering CR, Zhou JH, Lee JJ, Drummond JA, Peng SA, Saade RE, Tsai KY, Curry JL, Tetzlaff MT, Lai SY, Yu J, Muzny DM, Doddapaneni H, Shinbrot E, Covington KR, Zhang J, Seth S, Caulin C, Clayman GL, El-Naggar AK, Gibbs RA, Weber RS, Myers JN, Wheeler DA and Frederick MJ. Mutational landscape of aggressive cutaneous squamous cell carcinoma. Clin Cancer Res 2014; 20: 6582-6592.

[15] Li YY, Hanna GJ, Laga AC, Haddad RI, Lorch JH and Hammerman PS. Genomic analysis of metastatic cutaneous squamous cell carcinoma. Clin Cancer Res 2015; 21: 1447-1456.

[16] Al-Rohil RN, Tarasen AJ, Carlson JA, Wang K, Johnson A, Yelensky R, Lipson D, Elvin JA, Vergilio JA, Ali SM, Suh J, Miller VA, Stephens PJ, Ganesan P, Janku F, Karp DD, Subbiah V, Mihm MC and Ross JS. Evaluation of 122 advanced-stage cutaneous squamous cell carcinomas by comprehensive genomic profiling opens the door to new routes to targeted therapies. Cancer 2016; 122: 249-257.

[17] Yilmaz AS, Ozer HG, Gillespie JL, Allain DC, Bernhardt MN, Furlan KC, Castro LT, Peters SB, Nagarajan P, Kang SY, Iwenofu OH, Olencki T, Teknos TN and Toland AE. Differential mutation frequencies in metastatic cutaneous squamous cell carcinomas versus primary tumors. Cancer 2017; 123: 1184-1193.

[18] Schwaederle M, Elkin SK, Tomson BN, Carter JL and Kurzrock R. Squamousness: next-generation sequencing reveals shared molecular features across squamous tumor types. Cell Cycle 2015; 14: 2355-2361.

[19] Neskey DM, Osman AA, Ow TJ, Katsonis P, McDonald T, Hicks SC, Hsu TK, Pickering CR, Ward A, Patel A, Yordy JS, Skinner HD, Giri U, Sano D, Story MD, Beadle BM, El-Naggar AK, Kies MS, William WN, Caulin C, Frederick M, Kimmel M, Myers JN and Lichtarge O. Evolutionary action score of TP53 identifies high-risk mutations associated with decreased survival and increased distant metastases in head and neck cancer. Cancer Res 2015; 75: 1527-36.

[20] Zhou G, Liu Z and Myers JN. TP53 mutations in head and neck squamous cell carcinoma and their impact on disease progression and treatment response. J Cell Biochem 2016; 117: 2682-2692.

[21] Lee JE, Wang C, Xu S, Cho YW, Wang L, Feng X, Baldridge A, Sartorelli V, Zhuang L, Peng W and Ge K. H3K4 mono- and di-methyltransferase MLL4 is required for enhancer activation during cell differentiation. Elife 2013; 2: e01503

[22] Li SS, Jiang WL, Xiao WQ, Li K, Zhang YF, Guo XY, Dai YQ, Zhao QY, Jiang MJ, Lu ZJ and Wan R. KMT2D deficiency enhances the anti-cancer activity of L48H37 in pancreatic ductal adenocarcinoma. World J Gastrointest Oncol 2019; 11: 599-621.

[23] Ford DJ and Dingwall AK. The cancer COMPASS: navigating the functions of MLL complexes in cancer. Cancer Genet 2015; 208: 178-191.

[24] Moore GE, Merrick SB, Woods LK and Arabasz NM. A human squamous cell carcinoma cell line. Cancer Res 1975; 35: 2684-2688.

[25] Rodriguez-Villanueva J and McDonnell TJ. Induction of apoptotic cell death in non-melanoma skin cancer by interferon-α. Int J Cancer 1995; 61: 110-114.

[26] Ng SB, Bigham AW, Buckingham KJ, Hannibal MC, McMillin MJ, Gildersleeve HI, Beck AE, Tabor HK, Cooper GM, Mefford HC, Lee C, Turner EH, Smith JD, Rieder MJ, Yoshiura K, Matsumoto N, Ohta T, Niikawa N, Nickerson DA, Bamshad MJ and Shendure J. Exome sequencing identifies MLL2 mutations as a cause of Kabuki syndrome. Nat Genet 2010; 42: 790-793.

[27] Cheon CK and Ko JM. Kabuki syndrome: clinical and molecular characteristics. Korean J Pediatr 2015; 58: 317-324.

[28] Bjornsson HT, Benjamin JS, Zhang L, Weissman J, Gerber EE, Chen YC, Vaurio RG, Potter MC, Hansen KD and Dietz HC. Histone deacetylase inhibition rescues structural and functional brain deficits in a mouse model of Kabuki syndrome. Sci Transl Med 2014; 6: 256ra135.

[29] Benjamin JS, Pilarowski GO, Carosso GA, Zhang L, Huso DL, Goff LA, Vernon HJ, Hansen KD and Bjornsson HT. A ketogenic diet rescues hippocampal memory defects in a mouse model of Kabuki syndrome. Proc Natl Acad Sci U S A 2017; 114: 125-130.

[30] Sun P, Wu T, Sun X, Cui Z, Zhang H, Xia Q and Zhang D. KMT2D inhibits the growth and metastasis of bladder cancer cells by maintaining the tumor suppressor genes. Biomed Pharmacother 2019; 115: 108924.

[31] Morcillo-Garcia S, Noblejas-Lopez MDM, Nieto-Jimenez C, Perez-Peña J, Nuncia-Cantarero M, Győrffy B, Amir E, Pandiella A, Galan-Moya EM and Ocana A. Genetic mutational status of genes regulating epigenetics: role of the histone methyltransferase KMT2D in triple negative breast tumors. PLoS One 2019; 14: e0209134.

[32] Lv S, Ji L, Chen B, Liu S, Lei C, Liu X, Qi X, Wang Y, Lai-Han Leung E, Wang H, Zhang L, Yu X, Liu Z, Wei Q and Lu L. Histone methyltransferase KMT2D sustains prostate carcinogenesis and metastasis via epigenetically activating LIFR and KLF4. Oncogene 2018; 37: 1354-1368.

[33] Xiong W, Deng Z, Tang Y, Deng Z and Li M. Downregulation of KMT2D suppresses proliferation and induces apoptosis of gastric cancer. Biochem Biophys Res Commun 2018; 504: 129-136.

[34] Maraver A, Fernandez-Marcos PJ, Cash TP, Mendez-Pertuz M, Dueñas M, Maietta P, Martinelli P, Muñoz-Martin M, Martínez-Fernández M, Cañamero M, Roncador G, Martinez-Torrecuadrada JL, Grivas D, de la Pompa JL, Valencia A, Paramio JM, Real FX and Serrano M. NOTCH pathway inactivation promotes bladder cancer progression. J Clin Invest 2015; 125: 824-830.

[35] Yao Y, Ni Y, Zhang J, Wang H and Shao S. The role of Notch signaling in gastric carcinoma: molecular pathogenesis and novel therapeutic targets. Oncotarget 2017; 8: 53839-53853.

[36] Oswald F, Rodriguez P, Giaimo BD, Antonello ZA, Mira L, Mittler G, Thiel VN, Collins KJ, Tabaja N, Cizelsky W, Rothe M, Kühl SJ, Kühl M, Ferrante F, Hein K, Kovall RA, Dominguez M and Borggrefe T. A phospho-dependent mechanism involving NCoR and KMT2D controls a permissive chromatin state at Notch target genes. Nucleic Acids Res 2016; 44: 4703-4720.

[37] Serrano MLA, Demarest BL, Tone-Pah-Hote T, Tristani-Firouzi M and Yost HJ. Inhibition of Notch signaling rescues cardiovascular development in Kabuki Syndrome. PLoS Biol 2019; 17: e3000087.

[38] Lin-Shiao E, Lan Y, Coradin M, Anderson A, Donahue G, Simpson CL, Sen P, Saffie R, Busino L, Garcia BA, Berger SL and Capell BC. KMT2D regulates p63 target enhancers to coordinate epithelial homeostasis. Genes Dev 2018; 32: 181-193.

[39] Kommagani R, Leonard MK, Lewis S, Romano RA, Sinha S and Kadakia MP. Regulation of VDR by deltaNp63alpha is associated with inhibition of cell invasion. J Cell Sci 2009; 122: 2828-2835.

[40] Chen Y, Liu X, Zhang F, Liao S, He X, Zhuo D, Huang H and Wu Y. Vitamin D receptor suppresses proliferation and metastasis in renal cell carcinoma cell lines via regulating the expression of the epithelial Ca2+ channel TRPV5. PLoS One 2018; 13: e0195844.

[41] Horas K, Zheng Y, Fong-Yee C, Macfarlane E, Manibo J, Chen Y, Qiao J, Gao M, Haydar N, McDonald MM, Croucher PI, Zhou H and Seibel MJ. Loss of the vitamin D receptor in human breast cancer cells promotes epithelial to mesenchymal cell transition and skeletal colonization. J Bone Miner Res 2019; 34: 1721-1732.

[42] Pacelli C, Adipietro I, Malerba N, Squeo GM, Piccoli C, Amoresano A, Pinto G, Pucci P, Lee JE, Ge K, Capitanio N and Merla G. Loss of function of the gene encoding the histone methyltransferase KMT2D leads to deregulation of mitochondrial respiration. Cells 2020; 9: 1685.